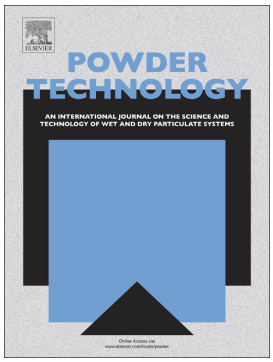


# Spray drying synthesis of silicon-enriched iron micro-powder (FeSi) for additive manufacturing and potential magnetic use

N. Somers, E. Erquiet, F. Cardillo, A. Mahmoud, R. Cloots, F. Boschini

PII: S0032-5910(26)00661-3

DOI: https://doi.org/10.1016/j.powtec.2026.122772

Reference: PTEC 122772

To appear in: *Powder Technology*

Received date: 18 March 2026

Revised date: 13 May 2026

Accepted date: 3 June 2026

Please cite this article as: N. Somers, E. Erquiet, F. Cardillo, et al., Spray drying synthesis of silicon-enriched iron micro-powder (FeSi) for additive manufacturing and potential magnetic use, *Powder Technology* (2024), https://doi.org/10.1016/j.powtec.2026.122772

# Spray drying synthesis of silicon-enriched iron micro-powder (FeSi) for additive manufacturing and potential magnetic use

N. Somers, E. Erquiet, F. Cardillo, A. Mahmoud, R. Cloots, F. Boschini

Affiliation : Group for Research in Energy and Environment from Materials (GREEnMat), University of Liège, Quartier Agora - B6a, Allée du Six-Août 13, 4000, Liège, Belgium

**Abstract**

Silicon steels, specifically Fe–6.5 wt% Si (Fe6.5Si), are essential for high-efficiency electrical machines due to their high magnetic permeability and near-zero magnetostriction. However, their extreme brittleness makes conventional processing difficult, driving the need for high-quality powders for additive manufacturing (AM) and powder injection molding (PIM). This study proposes a novel, sustainable and chemical synthesis route for silicon-enriched iron micro-powder (FeSi) powders combining ATEX-compliant spray drying with reductive calcination, utilizing recycled silicon sourced from end-of-life photovoltaic cells. The research systematically compares three iron precursors, iron nitrate ($Fe(NO_3)_3.9H_2O$), iron hydroxide ($Fe(OH)_3$) and iron oxide ($Fe_2O_3$) to determine their impact on powder morphology and yield. Spray drying parameters were optimized to produce spherical particles. Subsequent reductive calcination at 700°C for 6 hours under $Ar/H_2$ was found to be the critical threshold to achieve phase-pure FeSi. $Fe(OH)_3$ emerged as the superior precursor, providing the highest calcination yield (81%), the most robust spherical morphology and high chemical homogeneity, as confirmed by EDX mapping and Mössbauer spectroscopy. The successful incorporation of recycled PV-silicon establishes a lower-temperature, sustainable alternative to traditional gas atomization. These results demonstrate a versatile framework for producing high-performance soft magnetic powders with the flowability and structural integrity required for advanced manufacturing of electrical components.

**Keywords :** silicon iron, spray drying, LPBF, reductive calcination, synthesis, electrical machines

## 1. Introduction

Soft magnetic materials, defined by their low coercivity (<1000 A/m), are essential components in power generation, conditioning, conversion, and electromagnetic applications such as electric machines and transformers. Among various soft magnetic materials, silicon steels, particularly those containing around 3.2 wt% Si, dominate the market thanks to their balanced magnetic and mechanical properties, low cost, and excellent workability via conventional rolling processes [1–3].

However, growing demands for higher efficiency and reduced energy loss in electrical systems operating at medium to high AC frequencies have stimulated interest in high-silicon electrical steels, specifically Fe–6.5 wt% Si alloys (FeSi). These materials exhibit superior magnetic performance, including high resistivity, low iron loss, near-zero magnetostriction, and low magnetocrystalline anisotropy, making them ideal candidates for advanced applications in high-frequency motors, transformers, and magnetic shielding [1–3].

Despite their attractive properties, the widespread adoption of FeSi remains limited due to their intrinsic brittleness, caused by ordered B2 and D03 intermetallic phases [3], which renders them unsuitable for traditional cold rolling. Various alternative fabrication methods have been investigated, including warm rolling, strip casting, rapid solidification, chemical vapor deposition (CVD), and powder rolling. More recently, additive manufacturing (AM), particularly laser powder bed fusion (L-PBF), has emerged as a promising approach due to its high cooling rates ($\geq 10^4$ K/s), which can suppress phase ordering and mitigate embrittlement. AM also enables complex geometries and tailored microstructures that can further enhance magnetic performance [1–4].

To fully exploit AM for high-silicon steels, there is a growing need for metal powders with controlled composition, morphology, and flowability [4]. Close-coupled gas atomization (CCGA) [5] is currently the most widely used technique for producing spherical, high-purity metallic powders suited for AM, offering rapid solidification ($10^2$–$10^7$ K/s) and refined microstructures. However, challenges remain regarding cost, scalability, and sustainability, particularly for brittle or reactive materials like FeSi [1,4].

In this study, we propose an alternative synthesis route to conventional close-coupled gas atomization by employing an ATEX-compliant spray drying process using various liquid feedstocks. This approach operates at low temperature (typically below 300 °C), making it particularly well-suited for the synthesis of thermally sensitive materials, precursors, and alloys that are prone to oxidation or compositional segregation. By utilizing solution-, sol–gel-, or slurry-based precursors, spray drying enables enhanced molecular-level mixing, which facilitates excellent chemical homogeneity, even in complex multi-component or metastable systems. Furthermore, ATEX compliance ensures safe processing of combustible metal powders (e.g., Al, Ti, Mg) and organic solvent-based feeds, both of which present explosion risks under conventional conditions. The technique is used to produce fine powders, especially when coupled with post-processing treatments such as calcination or reduction, making it highly relevant for applications including powder injection molding (PIM) and additive manufacturing (AM), for example. Unlike gas atomization, which generally yields coarser particles unless followed by mechanical milling, spray drying can be readily tuned to generate tailored morphologies, including hollow, porous, or core–shell structures, through precise control over feed composition and drying parameters. Additionally, spray drying offers advantages in terms of versatility, scalability, process versatility, and cost-effectiveness, as it does not require high-temperature metal melting or high-pressure atomization nozzles, which are typical of gas atomization systems [6].

Inspired by the work of Jo *et al*. [7], who developed a scalable process for the fabrication of SiFeCNT secondary particles via spray drying of silicon and iron nitrate, this study investigates the synthesis of silicon-enriched iron micro-powder using an ATEX-compliant spray drying route. In contrast to conventional approaches, this method employs recycled silicon sourced from end-of-life photovoltaic (PV) cells in combination with three different iron precursors, aiming to develop a safer, scalable, lower-

temperature, and more sustainable pathway for powder synthesis. The spray-dried powders were subjected to reductive calcination, which was systematically optimized to yield well crystalline phase-pure FeSi while preserving particle integrity and morphology. The research focuses on comparing the use of three iron precursors, evaluating the feasibility of using recycled silicon in FeSi powder production, and assessing the potential of combining ATEX spray drying with reductive calcination as a versatile synthesis route. The resulting powders are characterized with regard to their suitability for a downstream application such as additive manufacturing, offering a promising pathway toward environmentally conscious and scalable production of functional FeSi powders. To the authors' knowledge, there are no studies reporting the synthesis of FeSi powder via ATEX spray drying process.

## 2. Experimental procedure

### 2.1. Synthesis of FeSi powders

Three different iron precursors are used in this study to synthetize FeSi powder: iron nitrate ($Fe(NO_3)_3.9H_2O$, Fischer Scientific, ≥98%), iron hydroxide ($Fe(OH)_3$, Fischer Scientific, ≥99%) and iron oxide ($Fe_2O_3$, Sigma-Aldrich, ≥96%). Silicon is coming from the recycling of end-of-life photovoltaic wafers, expertise from the GREEnMat laboratory [8]. As explained in a previous work, GREEnMat silicon recovery route consists of removing connections and conductive layers present in photovoltaic cells followed by ball milling to obtain ultrahigh purity nanosized Si powder [8]. Si suspensions in isopropanol (40 wt%) are used as raw materials. Polyvinyl pyrrolidone (PVP, Sigma-Aldrich, wt 360000) was used as binder using a 10 wt% solution in isopropanol (technical, VWR Chemicals, ≥ 98%).

Suspensions of the three iron precursors with 6.5 wt% of Si relative to the iron content are prepared in isopropanol (technical, VWR Chemicals, ≥ 98%). A constant agitation (stirring blade) is maintained during 12 hours prior to the spray drying. The final dry matter content of each suspension is 51.7 wt%. Composition of suspensions for each iron precursor before ATEX spray drying are shown in Table 1.

*Table 1 : Composition of suspensions for each iron precursor before ATEX spray drying.*

| Suspensions | Iron source | $Si_{PV}$ *(40 wt% in isopropanol)* | PVP (10 wt% in isopropanol) | Isopropanol |
|---|---|---|---|---|
| $Fe_2O_3$ | 46.5 wt% | 5.1 wt% | 1.9 wt% | 46.5 wt% |
| $Fe(OH)_3$ | 46.7 wt% | 4.7 wt% | 1.9 wt% | 46.7 wt% |
| $Fe(NO_3)_3.9H_2O$ | 48.5 wt% | 1.1 wt% | 1.9 wt% | 48.5 wt% |

The spray drying of suspensions is carried out with a Spray-dryer Niro Mobile Minor ATEX using the following optimized parameters: inlet temperature 140°C, outlet temperature ~81 °C, air pressure 1.6 bar, bi-fluid injector, and feed rate of 25 mL/min.

After spray drying, dried powders are calcined in flat alumina crucibles at 700°C during 6h under reductive atmosphere (95Ar/5$H_2$) in a GPCMA modified atmosphere chamber furnace (Carbolite) with a flow of 5L/min. This step is necessary to convert all iron precursors to metallic iron.
The commercial FeSi used as reference comes from m4p material solutions GmbH (Austria).

## 2.2. Characterizations of powders

Morphological properties and the particle size are characterized by scanning electron microscopy and laser diffraction granulometry. The composition of the material is investigated by X-ray diffraction technique. Finally, Mössbauer spectroscopy provides detailed information about the oxidation state, chemical environment and magnetic properties of the iron in the produced FeSi powders.

### 2.2.1. X-ray diffraction

X-ray diffraction measurements are performed in Bragg-Brentano geometry using a Bruker D8 Twin-Twin diffractometer with Cu $K_{alpha}$ radiation and Lynxeye XET 1D detector. Powders are analyzed over the 2θ range from 10° to 70°, with 0.2 s/channel step time and 15 rpm rotation speed. The whole powder pattern fitting procedure is performed using TOPAS and Profex [9] softwares. The fundamental parameters approach is used to describe the instrumental contribution [10]. The crystalline phases are identified using Joint Committee on Powder Diffraction International Centre for Diffraction Data (JCPDS-ICDD) files.

### 2.2.2. Laser diffraction granulometry

The particles are dispersed in isopropanol and the analysis is performed on Malvern Mastersizer 3000 Hydro.

### 2.2.3. Scanning electron microscopy

A field emission gun microscope TESCAN CLARA equipped with an energy dispersive X-ray spectroscopy (EDX) detector, processed under a 15 kV accelerating voltage and high vacuum, is used for the morphological characterization of spray dried powders before and after reductive calcination. The powders are deposited on carbon tapes. The sputtering deposition is done with a carbon target under vacuum (SPI-MODULE Carbon Coater, SPI Supplies).

### 2.2.4. Mössbauer spectroscopy

$^{57}$Fe Mössbauer spectroscopy analysis was conducted using 50 mCi rhodium matrix cobalt 57 source on a constant-acceleration spectrometer. The velocity of the measurements was ranged from +/- 12 mm/s. The Mössbauer spectral absorbers were prepared with ~40 mg $cm^{-2}$ of the material mixed with boron nitride. The magnetically split sextet spectrum of a high-purity α-Fe foil was used as a reference absorber to calibrate the spectrometer at ambient temperature. Hyperfine parameters like isomer shift

(δ), quadrupole splitting (Δ), linewidth (Γ) as well as the relative area of the various spectra components were obtained by fitting the experiment data using Fullham program.

#### 2.2.5. Flow performance of powders

The flow behavior of the powders was evaluated using a GranuDrum (Granutools, Belgium) instrument (84 mm diameter, 20 mm length), a rotating drum geometry designed to measure powder dynamics under gravity-induced stress [11,12] . The drum was half-filled with the powder sample and rotated around its central axis at angular velocities ranging from 5 to 40 rpm. To capture the flowing dynamics, the drum was back-lit by a stroboscope, and a CCD camera recorded the powder-air interface. For each imposed velocity, 50 images were captured at 0.5-second intervals. An edge-detection image-processing algorithm was utilized to identify the interface between the granular material (black) and air (white). From the captured frames, two primary rheological parameters were extracted based on the average of the 50 images: the flowing angle and the cohesive index. Measured at the center of the flow, the flowing angle represents the angle between the horizontal and the average interface position. The cohesive index is calculated as the standard deviation of the interface fluctuations and quantifies the cohesion within the drum [12].

The packing dynamics and tapped density were analyzed using the GranuPack ((Granutools, Belgium), an automated instrument designed to eliminate operator bias and ensure high reproducibility in density measurements [11–13]. The sample was subjected to successive taps, with the tube moving vertically over a height of 3 mm at a frequency of 1 Hz. After each tap, a distance sensor measures the height of the hollow cylinder to determine the powder's volume. The instrument then calculates the following key properties: bulk density (ρ[0]), tapped density after 500 taps (ρ[500]), Hausner ratio (Hr) and Carr's index (compressibility, C).

## 3. Results and discussion

XRD patterns of raw materials (iron sources and silicon from end-of-life photovoltaic wafers) used in the preparation of FeSi powders are illustrated in Figure 1 (a). It is clear that all the used precursor materials are pure without the presence of any secondary crystalline phase that might affect the final FeSi powders.

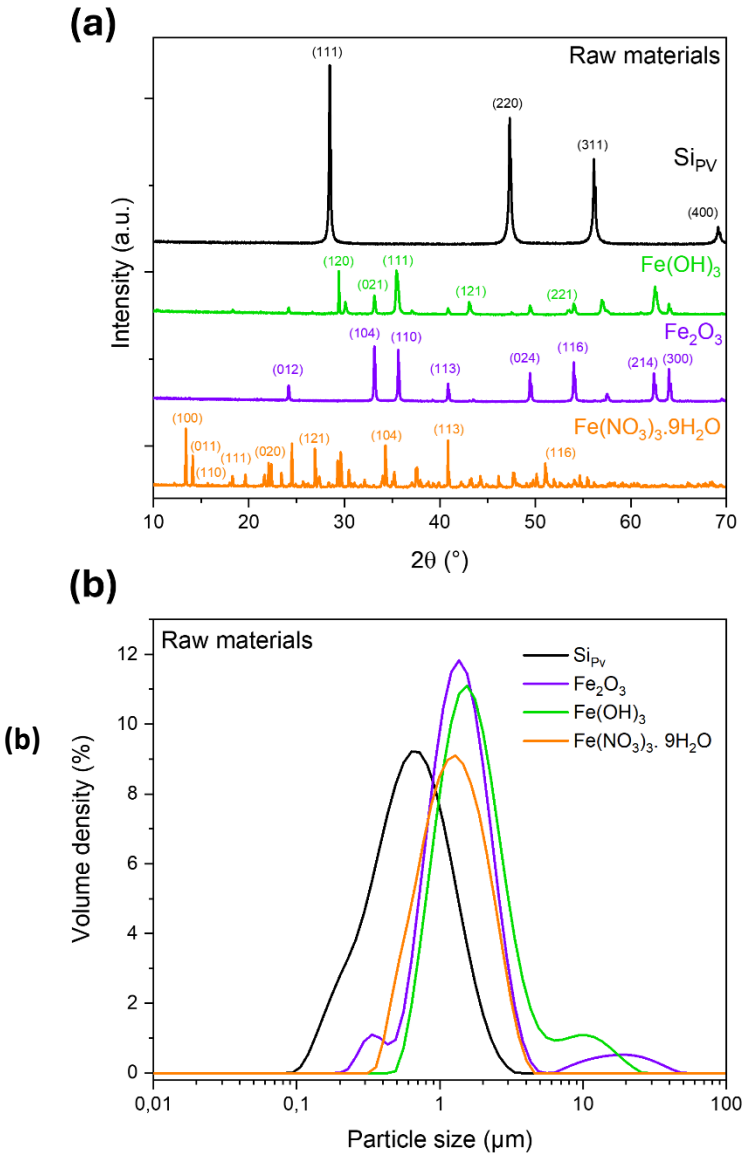


(b)

*Figure 1 : (a) X-ray diffractograms and (b) particle size distribution (in volume) of raw materials for the synthesis of FeSi powders.*

Particle size distributions of raw materials for the synthesis of FeSi powders are displayed in Figure 1 (b) and corresponding particle size values are grouped in Table 2.

The three iron precursors show relatively similar Dv(50) and D[4,3] values but slightly differ in terms of span of the particle size distribution. $Fe(NO_3)_3.9H_2O$ has a narrower and monomodal particle size distribution where $Fe(OH)_3$ and $Fe_2O_3$ exhibit bi-modal and tri-modal distributions, respectively. Silicon from end-of-life photovoltaic wafers shows a monomodal particle size distribution with Dv(50) and D[4,3] values below 1 µm, result of a previous milling step during the recovery of the silicon [8]. For all raw materials, the particle size is optimal for spray drying and the formation of the final phase with limited diffusion distances [14].

### 3.1 Spray drying

Spray drying yield is the ratio of recovered dry powder to the total solids in the feed. As seen in Table 3, yields for the different iron precursors are lower than the generally accepted optimum powder yield of 50% [15]. A low yield suggests difficulties in producing free-flowing powder due to stickiness during the process. Factors affecting yield include product stickiness, losses to chamber walls, and inefficient particle separation [15]. Optimization to avoid such stickiness involves controlling process parameters like inlet temperature, feed flow rate, and using techniques to prevent powder from sticking to the equipment. In future optimizations, anti-caking agents like hydrophilic or hydrophobized fumed silica could also be added to absorb moisture and prevent powder particles from sticking. The use of $Fe(NO_3)_3.9H_2O$ increases the stickiness more compared to the other two precursors, probably due to hygroscopic nature of nitrates leading to walls sticking. Smaller particles tend to be more numerous when using $Fe(NO_3)_3.9H_2O$ as the iron precursor, resulting from the slightly smaller particle size of the raw material and the partial dissolution of iron nitrate in isopropanol. There is no important difference in yield between $Fe_2O_3$ and $Fe(OH)_3$, where ratio between small and large particles are relatively similar. This is coherent with the particle size distribution of raw materials.

*Table 2 : Particle size values of raw materials for the synthesis of FeSi powders (particle size based on volume-weighted).*

| Raw materials | Dv(10) | Dv(50) | Dv(90) | D [4,3] |
|---|---|---|---|---|
| $Si_{Pv}$ | 0.25 µm | 0.62 µm | 1.36 µm | 0.73 µm |
| $Fe_2O_3$ | 0.70 µm | 1.37 µm | 2.74 µm | 2.26 µm |
| $Fe(OH)_3$ | 0.88 µm | 1.66 µm | 4.29 µm | 2.50 µm |
| $Fe(NO_3)_3.9H_2O$ | 0.66 µm | 1.31 µm | 2.55 µm | 1.48 µm |

*Table 3 : Spray drying yield for each type of suspension.*

| Suspensions | Yield of spray drying | Small particles (cyclone collector) | Large particles (primary collector) |
|---|---|---|---|
| $Fe_2O_3$ | 42.0% | 57.1% | 42.9% |
| $Fe(OH)_3$ | 42.2% | 55.5% | 44.5% |
| $Fe(NO_3)_3.9H_2O$ | 31.2% | 84.0% | 16.0% |

X-ray diffractograms of spray-dried powders before reductive calcination are shown in Figure 2. The spray-dried powder from $Fe(NO_3)_3.9H_2O$ precursor is quite amorphous with only a few diffraction peaks corresponding to silicon and silica. This amorphous nature is coherent with the study of Jo *et al.[7]*, highlighting the ability of nitrates to generate amorphous iron nitrate particles with spray-drying. Spray-dried powders from $Fe(OH)_3$ and $Fe_2O_3$ precursors are more crystalline and include several crystalline phases. For the spray-dried powder from the $Fe(OH)_3$ precursor, magnetite ($Fe_3O_4$) and hematite (α-

$Fe_2O_3$) phases are predominant with minor peaks of $Fe(OH)_3$ and silicon. On the other hand, the spray-dried powder from the $Fe_2O_3$ precursor, the major crystalline phase is hematite with minor peaks of silicon and magnetite. The formation of $SiO_2$ is primarily driven by the precursor chemistry and system pH. In the iron nitrate route, the highly acidic environment (pH < 2) catalyzes the hydrolysis and condensation of dissolved silicon species. This results in molecular-level mixing, where the silicon precipitates as a $SiO_2$ network throughout the iron matrix during the rapid evaporation of the spray-drying process. In contrast, mixtures involving iron oxides or hydroxides function as heterogeneous slurries at near-neutral or slightly basic pH levels. Under these conditions, the iron and silicon remain as distinct, insoluble solid phases with minimal chemical interaction. Consequently, no new silica phase is formed, and the components retain their separate physical identities throughout the drying process. This difference of composition can influence the reactivity during the reductive calcination since thermodynamics indicates that $Fe_2O_3$ is first reduced into $Fe_3O_4$, then FeO and finally Fe (above 550 °C) [16].

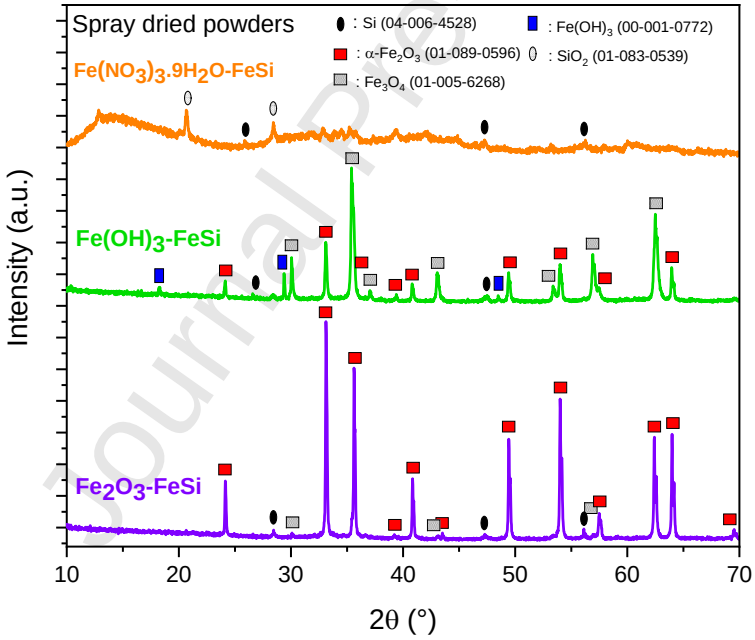


*Figure 2 : X-ray diffractograms of spray-dried powders before reductive calcination.*

Figure 3 (a) and (b) show particle size distributions of spray-dried powders before reductive calcination. Table 4 displays particle size values of spray-dried powders before reductive calcination.

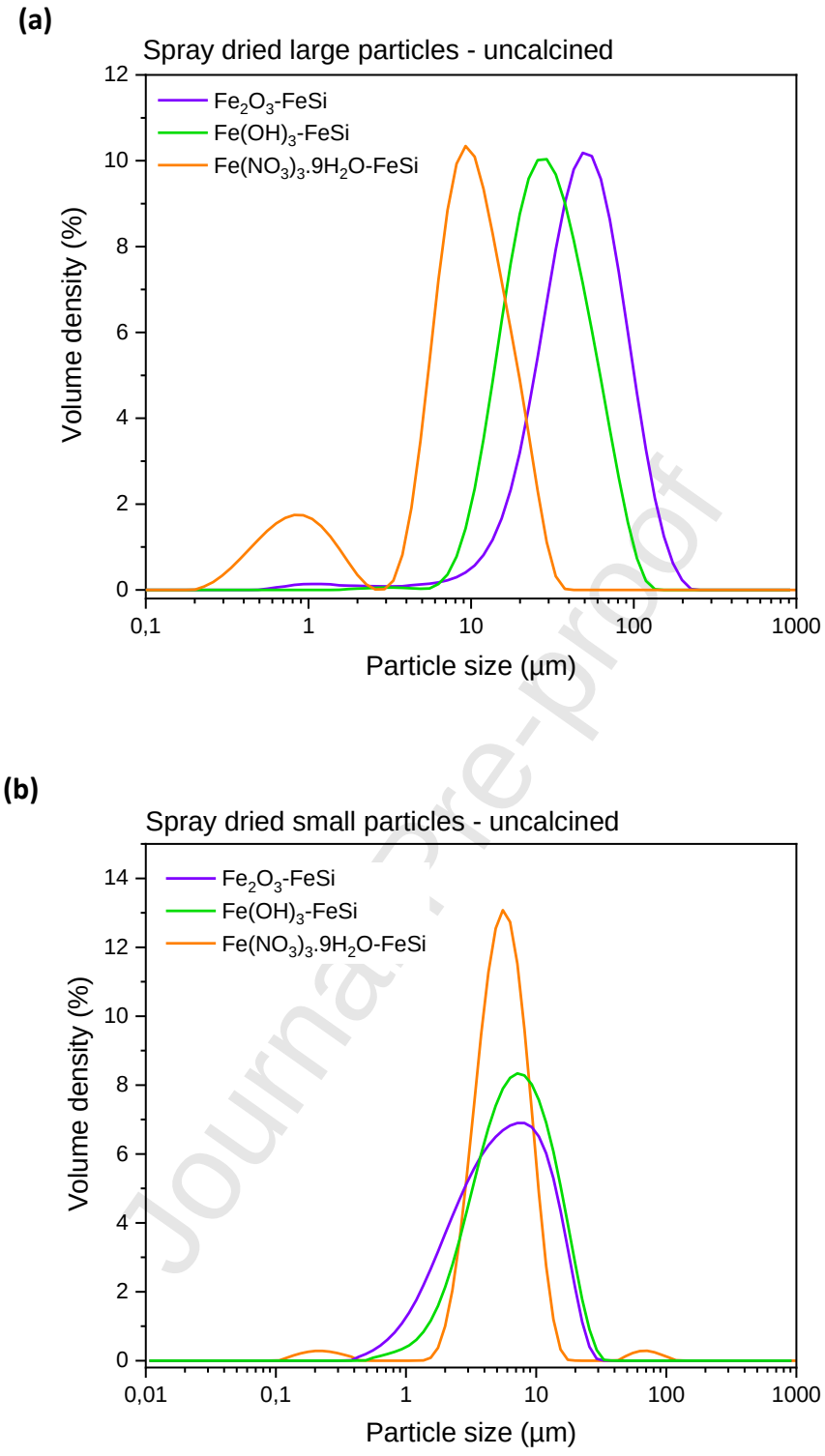


*Figure 3 : Particle size distributions of spray-dried powders before reductive calcination, (a) large particles (primary collector) and (b) small particles (cyclone collector).*

Regarding large particles (Figure 3 (a) and Table 4), the spray-dried powder from $Fe(NO_3)_3.9H_2O$ precursor shows a general smaller particle size with a bi-modal distribution centered at 9.9 µm. The powder issued from the $Fe_2O_3$ precursor presents the most important particle size distribution with a

Dv(50) of 48.0 µm compared to 28.8 µm for the powder from the $Fe(OH)_3$ precursor. This result could be explained by the partial dissolution of iron hydroxide in isopropanol, leading to smaller particles when dried by the gas flow.

About small particles (Figure 3 (b) and Table 4), the difference between iron precursors is significantly less pronounced with Dv(50) around 6 µm. $Fe_2O_3$ and $Fe(OH)_3$ powders present broad monomodal distributions, where the $Fe(NO_3)_3.9H_2O$ powder possesses a trimodal distribution with a narrow peak around 6 µm as well as two minor peaks at 0.2 µm and 70 µm. The separation of small particles during the spray drying process is more efficient than large particles (primary collector) due to the action of the cyclone.

Figure 4 presents a comparison of the spray-dried powders before reductive calcination from the three iron precursors (large particles).

*Table 4 : Particle size values of spray-dried powders before reductive calcination.*

| Compositions | Dv(10) | Dv(50) | Dv(90) | D [4;3] |
|---|---|---|---|---|
| Large $Fe_2O_3$-FeSi | 20.6 µm | 48.0 µm | 98.1 µm | 54.6 µm |
| Large $Fe(OH)_3$-FeSi | 13.8 µm | 28.8 µm | 61.6 µm | 33.8 µm |
| Large $Fe(NO_3)_3.9H_2O$-FeSi | 0.9 µm | 9.1 µm | 18.8 µm | 9.9 µm |
| Small $Fe_2O_3$-FeSi | 1.7 µm | 5.5 µm | 14.2 µm | 6.9 µm |
| Small $Fe(OH)_3$-FeSi | 2.6 µm | 6.7 µm | 15.5 µm | 8.0 µm |
| Small $Fe(NO_3)_3.9H_2O$-FeSi | 3.0 µm | 5.5 µm | 9.6 µm | 6.6 µm |

Regarding the $Fe_2O_3$-based powder (Figure S1 and Figure 4 (a) to (c)), the large particles are well-formed spheres, characteristic of powders produced by methods like spray drying where liquid droplets solidify. Figure 4 (c) provides a high-magnification view of one such large aggregate (diameter of approximately 14 µm), where it confirms that the spherical particle is a secondary structure built from the aggregation of many primary nanoparticles (<1 µm). The surface of the large spheres is rough and porous, confirming the granular nature of the constituent nanoparticles. Small Particles (Figure S1 (d) to (f)) consist primarily of irregularly shaped aggregates, almost without any distinct, large, well-formed spheres seen in the "Large particles" set. The aggregates formed are much smaller (sub-micron to a few micrometers) and less compact than the "Large particles" spheres, appearing as loose clusters or flocks.

For $Fe(OH)_3$-based powders, large particles (Figure S2 and Figure 4 (d) to (f)) appear to be spherical aggregates with most being in the micron size range (diameters ranging from approximately 17 to 27 µm). Figure 4 (f) shows a high-magnification view of a single large spherical particle, revealing that it is composed of many much smaller primary nanoparticles that have aggregated together during the spray drying process. This is characteristic of powders produced by spray-drying a suspension or solution. Small particles (Figure S2 (d) to (f)) exhibit a much less defined spherical morphology and appear to be

more irregularly shaped aggregates with a broader size distribution. Figure S2 (f) shows a high-magnification view, confirming that the composition of these aggregates is also of nanoparticles, similar to the large particles, but the overall secondary structure is far less dense and spherical. Both the large and small aggregates show a rough surface texture due to the presence of the constituent nanoparticles that make up the final spray-dried particle.

For both $Fe_2O_3$- and $Fe(OH)_3$-based powders, large particles clearly have a much higher proportion of particles in the range of tens of micrometers, with well-formed, dense, spherical secondary structures. On the other side, small particles exhibit a much smaller effective aggregate size, with significant presence of fine, less-structured powder. The visible aggregates are less distinct and more clustered/agglomerated, suggesting different drying kinetics with a high degree of fragmentation led to a change in the final powder structure and size distribution.

The SEM micrographs for the $Fe(NO_3)_3.9H_2O$-based powder are slightly different (Figure S3 and Figure 4 (g) to (i)). The most striking feature across all panels is the highly porous, clustered, and flower-like nature of the aggregates. They are not the dense, compact spheres seen in Figure 4 (a) to (c) and Figure 4 (d) to (f). High-magnification views (Figure 4 (h) and (i)) clearly show that each larger particle is a loose aggregate of smaller, roughly spherical or sub-micron-sized primary crystallites that are weakly bound together. The lack of dense, smooth, perfectly spherical secondary particles suggests that the drying process was not optimized to involve the rapid atomization and surface tension effects of typical spray drying that create dense beads. These micrographs are characteristic of a hydrated salt that has been processed from an aqueous solution. The main difference between the “Large particles” and the "Small particles " could be the speed of the drying process where “small particles” exhibit a faster drying rate leading to smaller, less-cohesive aggregates and the "Large particles" show a slower drying process, allowing the primary crystallites more time to coalesce into larger, slightly denser clusters. The prominent "grape cluster" or "fluffy" morphology is the defining characteristic of this $Fe(NO_3)_3.9H_2O$-based powder (Figure 4 (g) to (i)), distinguishing it significantly from the solid spherical aggregates of the iron oxide (Figure 4 (a) to (c)) and hydroxide (Figure 4 (d) to (f)).

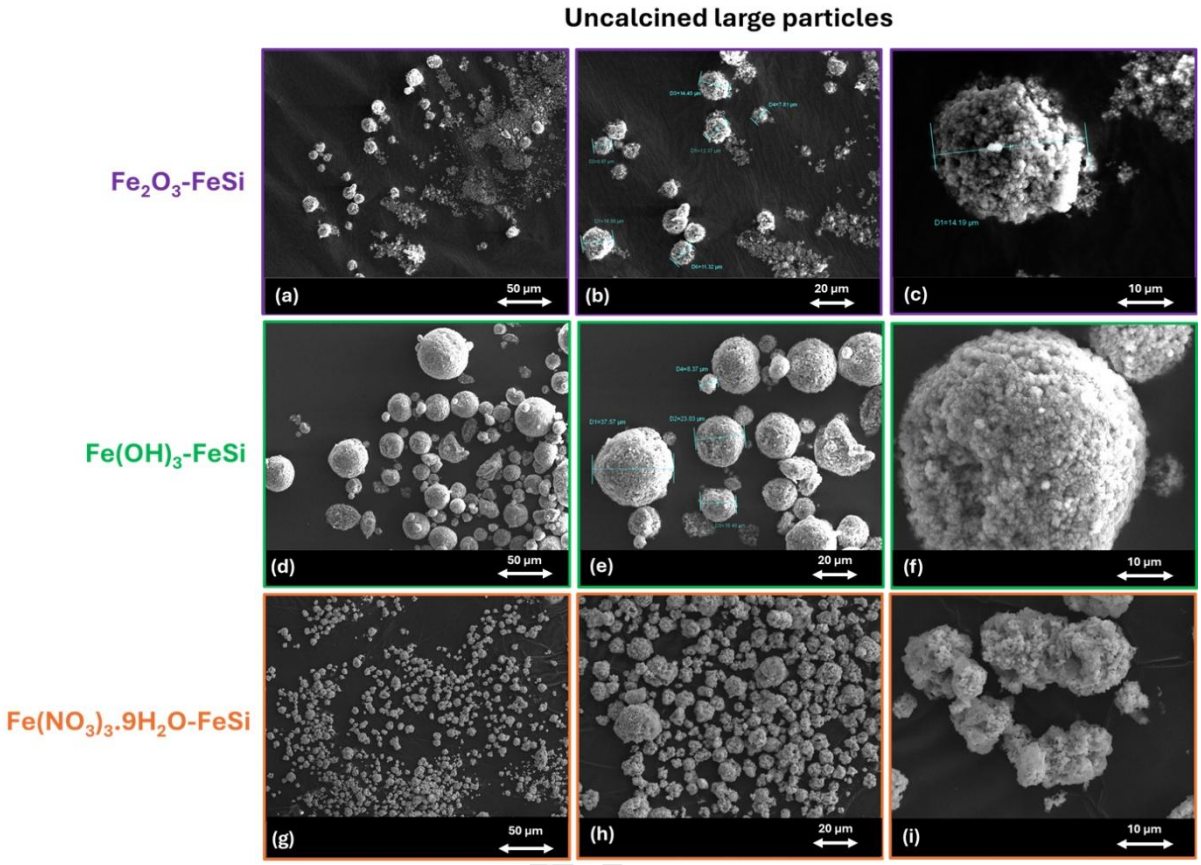


*Figure 4 : Micrographs of spray-dried powders before reductive calcination from the three iron precursors (only large particles). (a) to (c) $Fe_2O_3$-FeSi; (d) to (f) $Fe(OH)_3$-FeSi and (g) to (i) $Fe(NO_3)_3.9H_2O$-FeSi.*

The formation of spherical particles during spray drying is a result of the competition between evaporation kinetics, surface tension, and solute diffusion [14,17]. The process begins by forcing the liquid precursor (solution or slurry) through a nozzle, creating a fine mist of droplets. As soon as these droplets encounter the hot drying gas, surface tension acts to minimize the surface area for a given volume, naturally pulling the liquid into a spherical shape. In the initial stage, the droplet is saturated with moisture. Evaporation occurs at the surface at a constant rate, and the droplet temperature remains relatively low due to evaporative cooling. As solvent leaves (isopropanol here) the surface, the concentration of dissolved solids (iron precursors and silicon) increases at the droplet's periphery. As the solids concentration at the surface reaches a critical point, a solid shell or "crust" forms. Once the crust is established, the internal moisture must now diffuse through this solid shell to evaporate. Capillary forces pull the remaining liquid and smaller particles toward the shell, often leaving the center of the particle hollow or porous [14,17]. For both $Fe_2O_3$- and $Fe(OH)_3$-based powders, large particles form well-formed, dense, spherical particles. The shell is permeable and strong, allowing particles to remain solid-looking spheres that are not hollow (Figure 5). The nano-sized voids on the surface are likely the result of gas escaping through the crust. Regarding the $Fe(NO_3)_3.9H_2O$-based powder, the shell might have been too thin so the internal vacuum created by drying may have caused spheres to

collapse, leading to loose aggregate of smaller, roughly spherical primary crystallites that are weakly bound together.

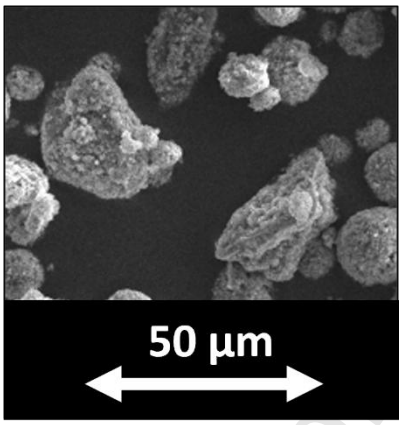


*Figure 5 : Micrograph zoom of a spray-dried powder before reductive calcination ($Fe(OH)_3$-FeSi).*

The scalability of the proposed method is supported by the inherent tunability of spray-drying parameters. Particle size can be precisely controlled by adjusting the atomization pressure, the solids concentration of the precursor solution, and the drying temperature. In this study, parameters were optimized for micron-sized powders, but the process can be shifted toward sub-micron or larger ranges by increasing the gas-to-liquid ratio or decreasing the feed concentration, respectively.

### 3.2 Reductive calcination

Table 5 displays the calcination yield in a reducing atmosphere for the different powder compositions. The use of $Fe(NO_3)_3.9H_2O$ as iron precursor leads to significant drop of calcination yield compared to the two other precursors with only 41%. This is due to the high amount of nitrate relative to the iron content in the iron nitrate precursor (theoretically only 13,82g of iron for 100g of $Fe(NO_3)_3.9H_2O$) which is then pyrolyzed during calcination. The highest calcination yield of the $Fe(OH)_3$ precursor probably comes from its chemical composition with the presence of both magnetite ($Fe_3O_4$) and hematite ($\alpha$-$Fe_2O_3$) phases in the spray dried powder. As explained at Figure 2, the major crystalline phase for the $Fe_2O_3$ precursor is $\alpha$-$Fe_2O_3$ which has to be reduced to $Fe_3O_4$ then FeO to the final $\alpha$-Fe phase. Since a fraction of the powder from the $Fe(OH)_3$ precursor is $Fe_3O_4$, the calcination yield is higher with less hematite phase to be reduced.

*Table 5 : Efficiency of reductive calcination for each iron precursor.*

| Compositions | Calcination yield |
|---|---|
| $Fe_2O_3$- FeSi | 72% |
| $Fe(OH)_3$- FeSi | 81% |
| $Fe(NO_3)_3.9H_2O$- FeSi | 41% |

Since the final target of this study is to produce FeSi powders for additive manufacturing, only powders fraction with large particles (yield in Table 3) have been studied after calcination for their promising particle size and flowability. Figure 6 shows X-ray diffractograms of spray-dried powders (large particles) after reductive calcination (700°C, 6h, 95Ar/5H2).

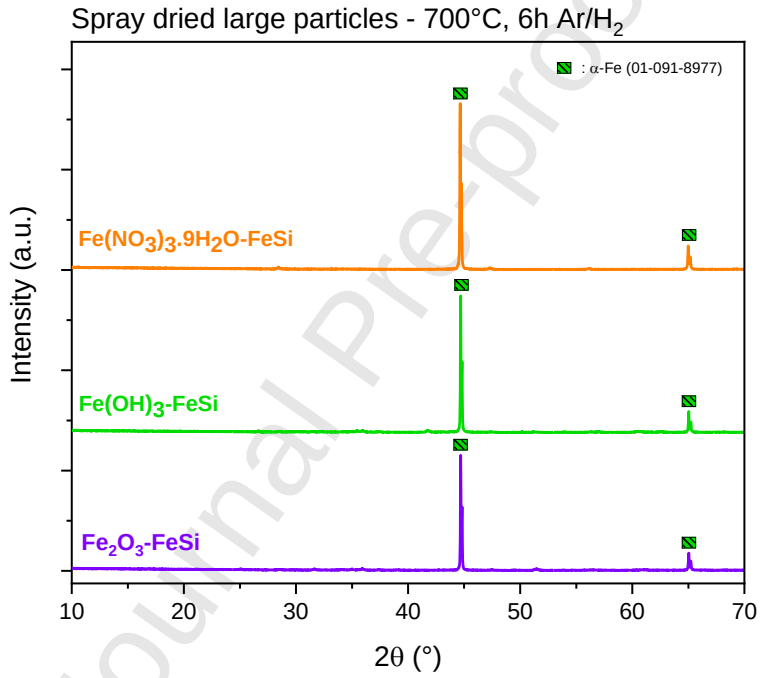


*Figure 6 : X-ray diffractograms of spray-dried powders (large particles) after reductive calcination (700°C, 6h, 95Ar/5H₂).*

Several optimizations were necessary to find the optimal thermal cycle in order to reduce all the oxides and to avoid any secondary phase. The major problem in these optimizations was the appearance of the fayalite phase ($Fe_2SiO_4$) which forms in a narrow range of oxygen pressures and temperature around 800-850°C [18–20]. The reaction between iron oxide and silicon can lead to fayalite according to equation (1) [21]:

$4\ Fe_2O_3 + 3\ Si \rightarrow Fe_2SiO_4 + 2\ Fe$

The presence of the $Fe_2SiO_4$ phase can alter the magnetic properties because it forms a thin insulating layer on the particles [21]. The reductive calcination should then occur at temperatures below 800°C to avoid the formation of fayalite and obtain pure FeSi powders. The duration of the thermal cycle has

to be long enough to reduce all oxide into metallic iron. A thermal treatment of six hours at 700°C with a flow of 95Ar/5$H_2$ (5L/min) allows the synthesis of pure FeSi powders without any secondary phase for all compositions (Figure 6).

The oxidation state, the local environment and magnetic behavior of Fe in the different FeSi samples were studied by $^{57}$Fe Mössbauer spectroscopy. Figure 7 depicts the transmission Mössbauer spectra recorded at room-temperature of the commercial and spray-dried powders after reductive calcination (700°C, 6h, 95Ar/5$H_2$). Their corresponding hyperfine parameters are summarized in Table 6. All spectra exhibit well-resolved sextets indicating that the materials are magnetically ordered at room temperature. For the commercial FeSi, a good-quality fit of its corresponding Mössbauer spectrum was obtained by using only two six-line patterns, corresponding to the alpha iron in FeSi. Indeed, the isomer shift, quadrupole spilling and magnetic field of the two sites is in good agreement alpha iron, the hyperfine field $B_{hf}$ values of two sites are different (31.3 and 27.6 T) the presence of two Fe(0) with different magnetic field indicates the presence of the random solid solution in the investigated material which is good agreement with results reported in the literature, L. Häggström *et al* confirmed this result in FeSi alloys with the composition range 0-25 % for Si [22]. Fe-site occupancies are obtained from Mössbauer sextet areas, assuming identical Lamb factors for all sites. The two sub-spectral components show different relative intensities of 62 and 38%. For the $Fe(OH)_3$-FeSi sample, the Mossbauer spectrum was also fitted using only two components, the two iron sites present relatively same hyperfine parameters as the commercial FeSi, which confirms the successful preparation of the FeSi from $Fe(OH)_3$. The only difference observed is that the two iron sites present different relative intensities (89 and 11% vs 62 and 38% for the commercial material) which can be explained by the formation of a different solution solid using $Fe(OH)_3$ precursors and spray drying method. For the $Fe_2O_3$- FeSi sample, the use of three components was necessary to obtain good quality fit of the spectrum: two sextets and one doublet. The two sextets present the same hyperfine parameters as for the commercial FeSi confirming the obtaining of the magnetic FeSi from $Fe_2O_3$. The third component (doublet) presents an isomer shift of 0.13 mm/s and a high quadrupole splitting of 1.74 mm/s corresponding to paramagnetic Fe(0) in high asymmetric environment which could correspond to amorphous or nanoparticles of Fe(0).

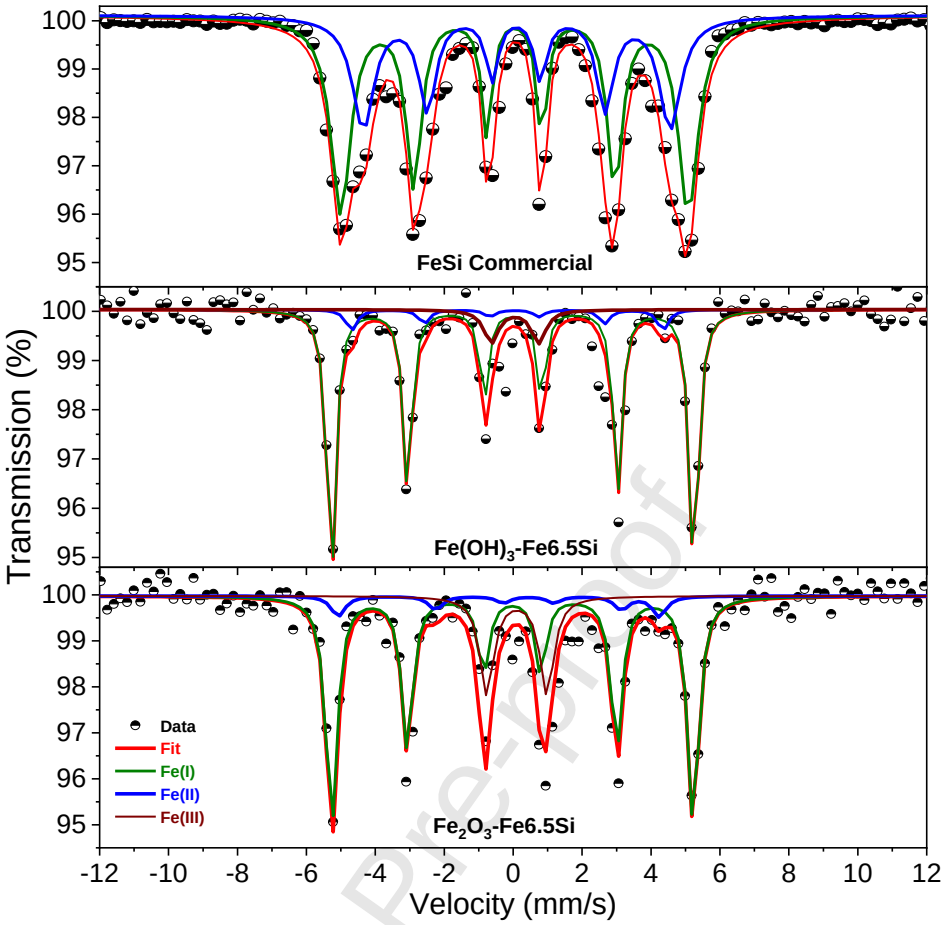


*Figure 7 : Mössbauer spectra recorded at room temperature of commercial and spray-dried FeSi powders after reductive calcination.*

*Table 6 : Mössbauer spectral parameters of commercial and spray-dried FeSi powders after reductive calcination.*

| | Parameters | FeSi Commercial | $Fe(OH)_3$-FeSi | $Fe_2O_3$- FeSi |
|---|---|---|---|---|
| **Fe(I)-magnetic** | **δ (mm/s)** | **0.04 (1)** | **0.01 (1)** | **-0.01 (1)** |
| | **Δ (mm/s)** | **0.00 (1)** | **0.00 (1)** | **0.01 (1)** |
| | **Γ (mm/s)** | **0.32 (1)** | **0.30 (1)** | **0.40 (1)** |
| | **Bhf (T)** | **31.3 (1)** | **32.3 (1)** | **32.6 (1)** |
| | **Area (%)** | **62 (1)** | **89 (1)** | **74 (1)** |
| **Fe(II)- Magnetic** | **δ (mm/s)** | **0.09 (1)** | **0.07 (1)** | **-0.02 (1)** |
| | **Δ (mm/s)** | **0.01 (2)** | **-0.21 (2)** | **-0.82 (2)** |
| | **Bhf (T)** | **27.6 (1)** | **28.1 (1)** | **28.9 (1)** |
| | **Γ (mm/s)** | **0.38 (1)** | **0.36 (1)** | **0.48 (1)** |
| | **Area (%)** | **38 (1)** | **11 (1)** | **7 (1)** |
| **Fe(II)-paramagnetic** | **δ (mm/s)** | | | **0.13 (1)** |
| | **Δ (mm/s)** | | | **1.74 (2)** |
| | **Γ (mm/s)** | | | **0.48 (1)** |
| | **Area (%)** | | | **19 (1)** |

In addition to these spectroscopic findings showing to the material's ferromagnetic potential, Figure 10 shows a photograph of the powder ($Fe(OH)_3$-FeSi particles) being attracted to a hand-held magnet.

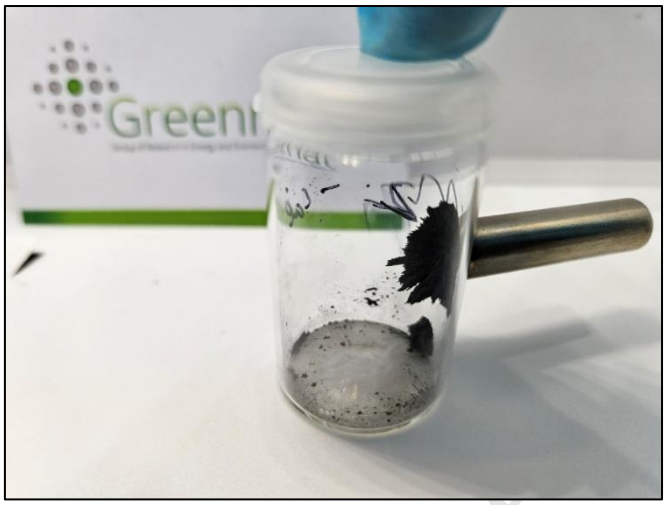

*Figure 8 : Photograph of the powder being attracted to a hand-held magnet, showing the ferromagnetic character of the as-synthetized powder ($Fe(OH)_3$-FeSi particles).*

Particle size distributions of spray-dried powders (large particles) after reductive calcination (700°C, 6h, $95Ar/5H_2$) are shown at Figure 9 and particle size values are displayed in Table 7.

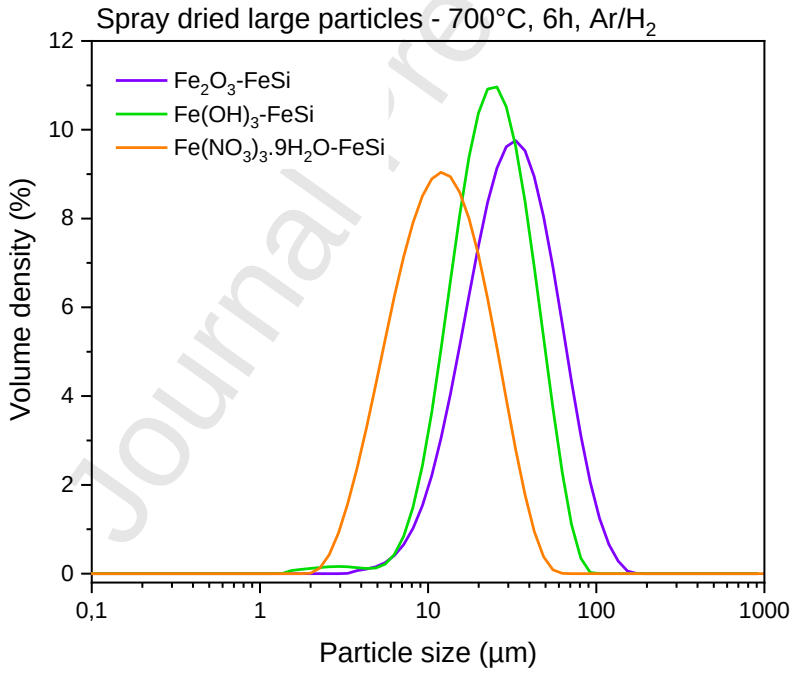


*Figure 9 : Particle size distributions of spray-dried powders (large particles) after reductive calcination (700°C, 6h, $95Ar/5H_2$).*

Regarding large particles from $Fe(NO_3)_3.9H_2O$ precursor, the initial bi-modal distribution prior calcination has turned into a mono-modal distribution where submicronic particles have agglomerated due to the increase of temperature. This leads to an increased Dv(50) of 11.7 µm instead of 9.9 µm before thermal treatment. For both $Fe_2O_3$-and $Fe(OH)_3$-based powders, a slight decrease in particle size is observed with a Dv(50) going from 48.0 µm to 31.4 µm and from 28.8 µm to 23.9 µm,

respectively. The densification generated by the heat treatment leading to a pre-sintering of the powders is the cause of this decrease in particle size. Powders issued from $Fe_2O_3$ and $Fe(OH)_3$ precursors present suitable properties for use in shaping processes such as powder injection molding (PIM) and additive manufacturing, where powders must be fine (typically < 45 µm) and spherical to ensure good flowability [4,23,24].

*Table 7 : Particle size values of spray-dried powders (large particles) after reductive calcination (700°C, 6h, 95Ar/5$H_2$).*

| Compositions | Dv(10) | Dv(50) | Dv(90) | D [4;3] |
|---|---|---|---|---|
| Large calcined $Fe_2O_3$-FeSi | 13.8 µm | 31.4 µm | 66.4 µm | 36.5 µm |
| Large calcined $Fe(OH)_3$-FeSi | 11.7 µm | 23.9 µm | 46.4 µm | 26.8 µm |
| Large calcined $Fe(NO_3)_3.9H_2O$-FeSi | 5,07 µm | 11.7 µm | 25.9 µm | 13.9 µm |

Micrographs of spray-dried powders (large particles) after reductive calcination (700°C, 6h, 95Ar/5H2) are visible at Figure 10.

The starting large particles of $Fe_2O_3$-based powder (Figure 10 (a) to (c)) have largely maintained their spherical shape acquired by the spray drying but have undergone significant microstructural change after reductive calcination. Figure 10 (c) shows that the sphere's surface is now highly porous, spongy, or honeycombed. This is a classic result of topochemical reduction where the reducing gas $H_2$ converts $Fe_2O_3$ to $Fe_3O_4$ to FeO to Fe. The volume change associated with the removal of oxygen atoms, coupled with the high temperature, causes pore formation and the creation of a pre-sintered network of nano-crystallites (metallic Fe) on the particle surface.

Regarding the $FeOH_3$-based powder (Figure 10 (d) to (f)), this material exhibits the best retention of the original spherical secondary particle structure. Indeed, Figure 10 (f) shows large, well-formed spherical particles, even denser than the $Fe_2O_3$-based product. The surface is rough, composed of many smaller units, but the overall structure is very robust. The $Fe(OH)_3$ precursor likely decomposed and densified to an oxide $Fe_2O_3$ at a lower temperature before the reduction began, forming highly stable secondary particles that were less prone to fragmentation or collapse during the reduction process, showing excellent structural stability under these conditions. The size is mostly similar with a diameter of approximately 25 µm.

The $Fe(NO_3)_3.9H_2O$-based powder, which was a loose, fluffy, grape-cluster aggregate after spray drying, shows complete collapse and fragmentation after the reductive calcination. The resulting powder (Figure 10 (g) to (i)) consists of small, irregular, poorly defined aggregates and fine particles. The high temperature likely caused the nitrate salt to melt, decompose violently, and rapidly release large amounts of gas ($NO_x$ and $H_2O$), leading to the destruction of the initial loosely bound structure. This morphology suggests the worst particle stability among the three precursors, resulting in a fine,

potentially dusty, and low-density product, which is often undesirable for high-temperature reduction processes. The image clearly demonstrates the profound influence of the initial precursor material and its preparation method on the final product morphology after high-temperature, gas-phase processing. First, $Fe(OH)_3$-derived particles show the most robust spherical morphology. Second, $Fe_2O_3$-derived particles maintain the sphere but exhibit high porosity from the reduction reaction. Finally, $Fe(NO_3)_3.9H_2O$-derived material suffers complete structural collapse and forms fine, irregular aggregates.

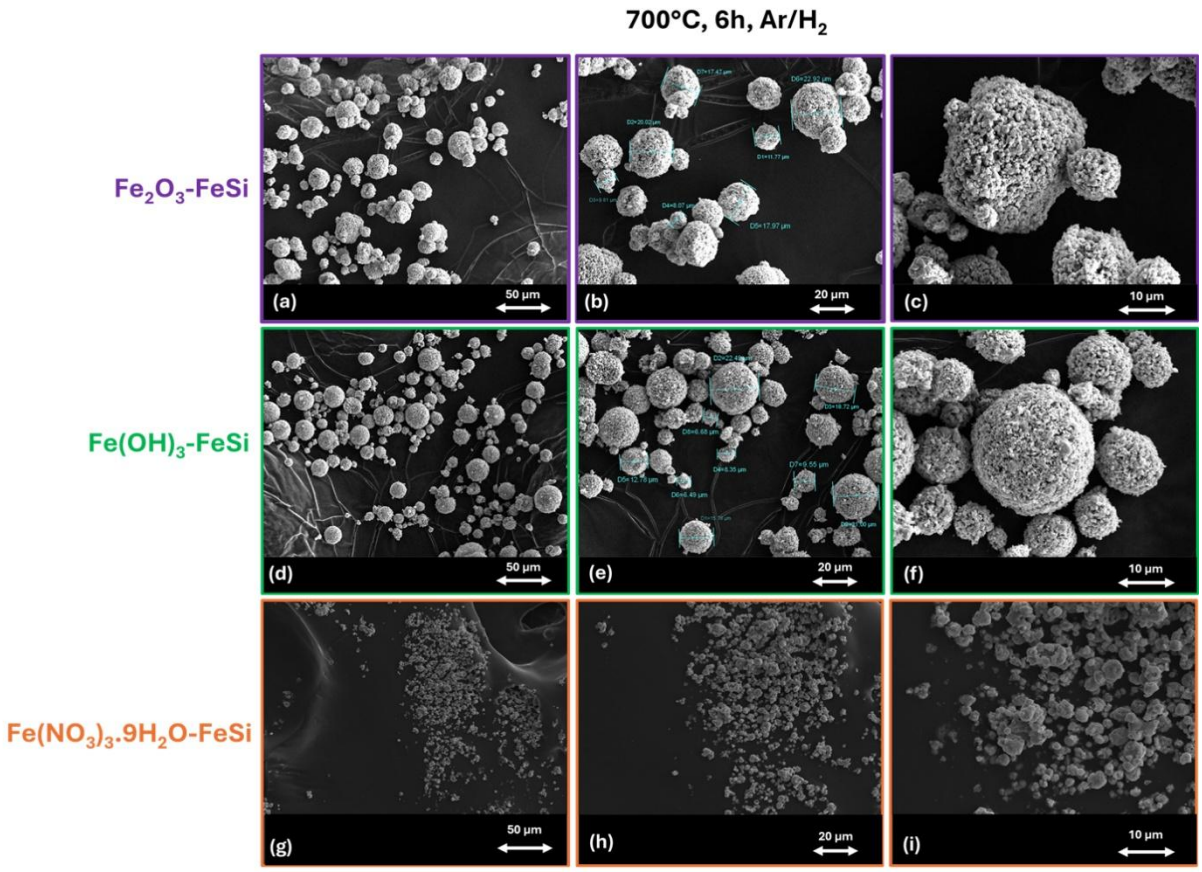


*Figure 10 : Micrographs of spray-dried powders (large particles) after reductive calcination (700°C, 6h, 95Ar/5$H_2$).*

Figure 11 shows EDX analysis and mapping of spray-dried powders (large particles) after reductive calcination (700°C, 6h, 95Ar/5H2). Table 8 displays EDX elementary composition of spray-dried powders (large particles) after reductive calcination. EDX spectra are a plot of X-ray count intensity versus X-ray energy and acts as the chemical "fingerprint" of the sample, providing quantitative elemental composition. Spectra from the three different powders have two dominant characteristic X-ray peaks: the Fe Kα peak at approximately 6.4 keV and the Si Kα peak at approximately 1.74 keV. Minor peaks can also be observed like oxygen Kα (0.52 keV) and other trace elements such as aluminum or contaminants from the starting materials or processing environment.

The maps visually represent the spatial distribution of each major element across the micrographs, revealing the homogeneity of the alloy. Regarding iron maps (red), they show a uniform distribution of iron across the entire scanned particle area, indicating that iron is the primary constituent. Silicon maps also show a highly uniform distribution of silicon throughout the particles, confirming that the Si is successfully incorporated into the Fe matrix (forming the α-Fe(Si) solid solution) rather than being segregated or clustered.

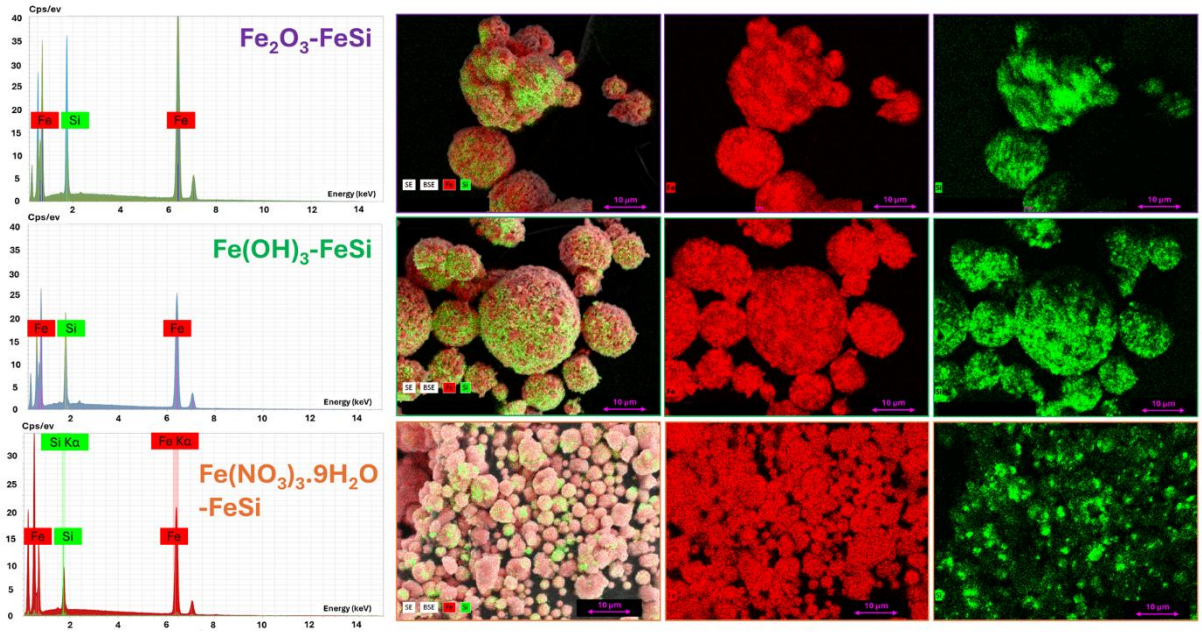


*Figure 11 : EDX analysis and mapping of spray-dried powders (large particles) after reductive calcination (700°C, 6h, 95Ar/5$H_2$).*

Table 8 displays the elemental composition in weight percent for the scanned area. For the FeSi alloy, the key result is the weight percentage of silicon, which should be close to 6.5wt% in the final powder for its magnetic properties. The powders derived from $Fe(OH)_3$ and $Fe_2O_3$ precursors achieve an identical, higher Si content of 9.4 wt%. The powder derived from the $Fe(NO_3)_3.9H_2O$ precursor results in a lower Si content of 8.2wt%. For all powders, silicon seems to have been introduced in excess compared to the target value of 6.5wt%. However, standard deviation values are quite high and similar for three materials (approximately 3%) covering a broad range of Si content. This also suggests that none of the precursors offered a distinct advantage in terms of significantly improving elemental homogeneity at this bulk composition. Further quantitative elemental characterization will be required to complete EDX results. ICP-MS (Inductively Coupled Plasma - Mass Spectrometry), for example, could bring more sensitivity and is ideal to determine the total concentration of elements in a sample. The next step of this work will be to connect FeSi powders stoichiometrically to experimental synthesis parameters and their final magnetic properties (e.g. magnetostriction and electrical resistivity).

*Table 8 : EDX elementary composition of spray-dried powders (large particles) after reductive calcination (700°C, 6h, 95Ar/5$H_2$). Average on 9 measurements in 3 different areas.*

| Compositions | (Fe (wt%) | Si (wt%) | Standard deviation |
|---|---|---|---|
| Large calcined $Fe_2O_3$-FeSi | 90.6% | 9.4% | 3.4 |
| Large calcined $Fe(OH)_3$-FeSi | 90.6% | 9.4% | 3.2 |
| Large calcined $Fe(NO_3)_3.9H_2O$-FeSi | 91.7% | 8.2% | 3.1 |

Regarding physical properties of particles, a comparison is made between a commercial FeSi powder (m4p, used for LPBF printers) and a synthesized powder issued from the GREEnMat lab (large calcined $Fe(OH)_3$-FeSi particles). This latter was chosen due to its interesting morphological properties and magnetic properties.

Figure 12 displays the snapshots of the powder-air interface for both samples at low (5 rpm) and high (40 rpm) rotating speeds. The green area represents the fluctuations of the interface over time, which is the visual manifestation of the Cohesive Index. The commercial powder exhibits a significantly thicker and more irregular green band across all speeds, particularly at 40 rpm. This suggests a "slumping" or "intermittent" flow regime, typical of materials with higher internal friction or inter-particle forces [12,13]. The GREEnMat powder maintains a thinner, more defined interface. This indicates a more stable and continuous flow, suggesting superior surface properties or a more optimized particle size distribution compared to the commercial counterpart.

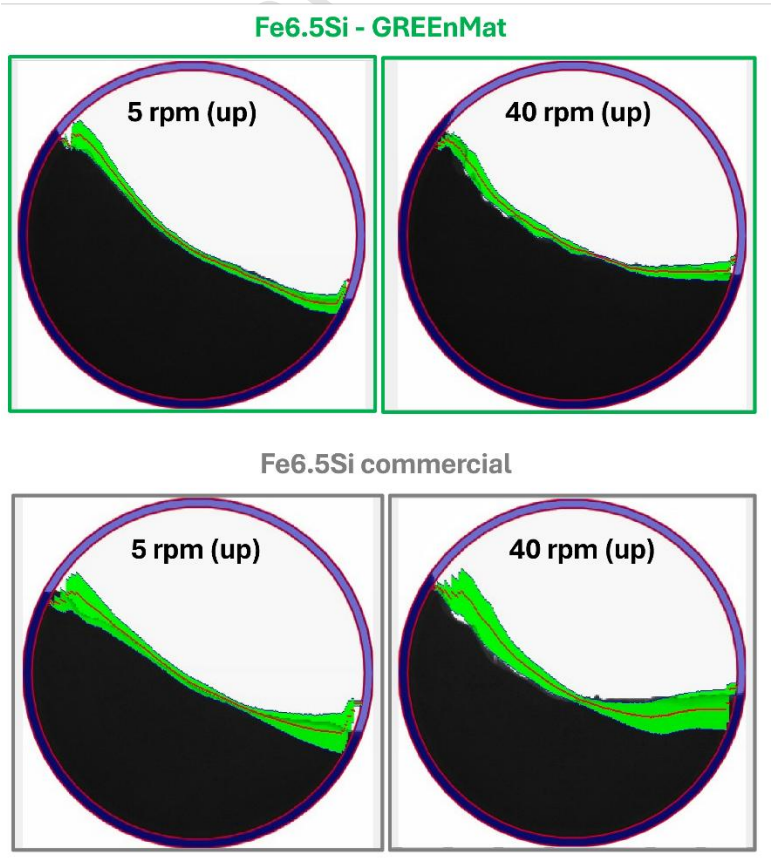

*Figure 12 : Pictures of the powders (GREEnmat (large calcined $Fe(OH)_3$-FeSi particles) and commercial) flowing in the drum at different speeds*

The evolution of the cohesive index as a function of rotating speed is presented in Figure 13 (a). The GREEnMat powder consistently exhibits a lower cohesive index than the commercial powder across the entire speed range (5–40 rpm). For both powders, the cohesion is not constant. The commercial powder shows a sharp increase in cohesion as speed increases beyond 25 rpm, likely due to the transition into a more chaotic flow regime [12]. In contrast, the GREEnMat powder remains relatively stable, with its cohesion values staying below 20, whereas the commercial powder peaks above 30. The lower cohesive index for GREEnMat implies that it is significantly less cohesive. This is a critical advantage for additive manufacturing or powder metallurgy applications, as it suggests better spreadability and reduced risk of clogging during powder handling [12,13].

The flow angle results in Figure 13 (b) provide further insight into the dynamic friction of the powders. At lower speeds (5–15 rpm), the GREEnMat powder displays a slightly higher flow angle 31-32°)compared to the commercial powder (26-31°). However, as the rotating speed increases, the flow angle for GREEnMat drops more significantly than the commercial sample, reaching its lowest point at 40 rpm. While a higher flow angle often suggests higher friction, the fact that GREEnMat combines a higher angle with a much lower cohesive index suggests a different packing state or "shear-thinning" behavior. The sharp decrease in flow angle for GREEnMat at high speeds indicates that once the material is in motion, it flows with less resistance than the commercial powder [12].

The combined data from Figure 13 confirms that FeSi GREEnMat possesses superior dynamic flow properties. The significantly lower cohesive index is the dominant factor here. While the flow angles are somewhat comparable, the stability of the GREEnMat interface (low cohesive index) proves that its flow is more laminar and predictable. This behavior is likely attributed to better particle morphology (sphericity). Consequently, the GREEnMat powder is expected to perform more reliably in industrial processes requiring rapid and uniform powder layering [12,13].

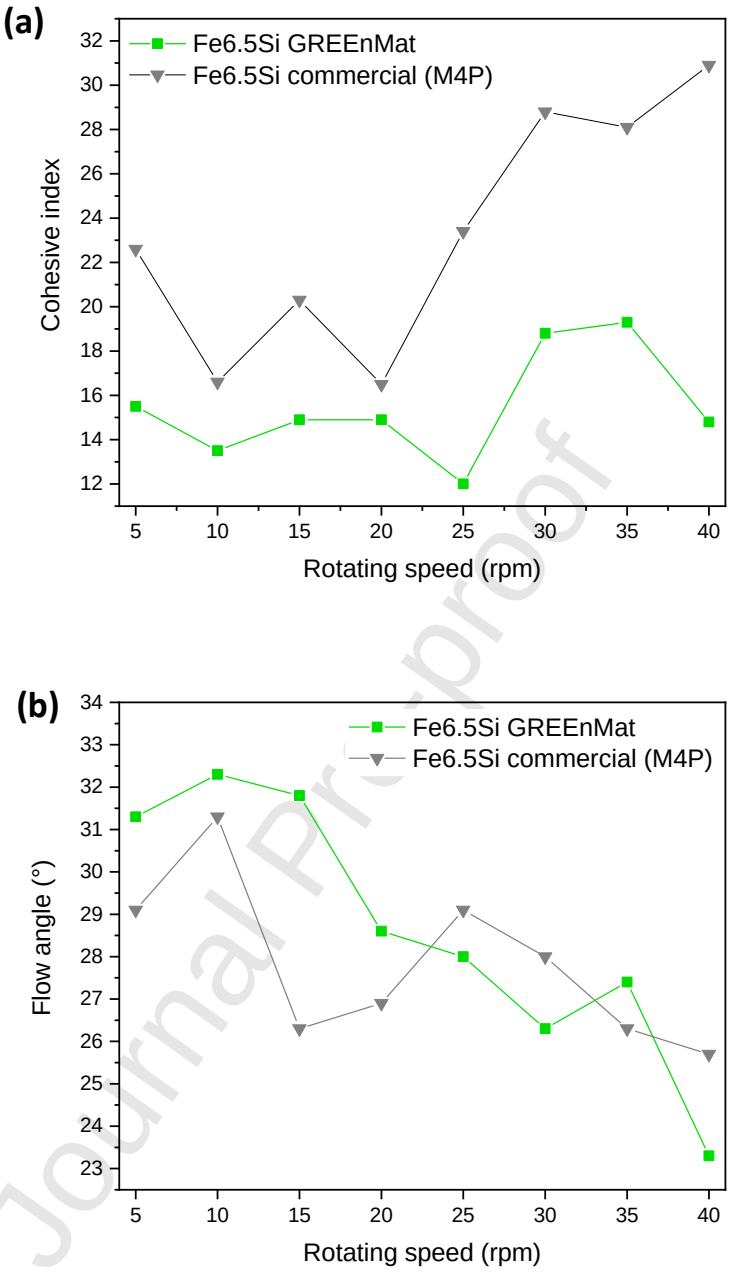


*Figure 13 : (a) Dynamic cohesive index and (b) flow angle measured with GranuDrum as a function of the rotating speed for the GREEnMat and commercial FeSi powders.*

Figure 14 illustrates the density evolution over 500 taps.  and coefficients are expressed in Table 9. Both powders follow a typical logarithmic compaction trend, reaching a plateau (asymptotic density) well before the 500th tap. There is a significant difference in absolute density. The FeSi commercial powder is much denser (ρ[0] of 4.53 g/cm3) compared to the GREEnMat powder (ρ[0] of 0.94 g/cm³). This suggests a major difference in the core material structure, potentially indicating that the GREEnMat version is a composite, porous, or otherwise lighter variant of the silicon-steel alloy.

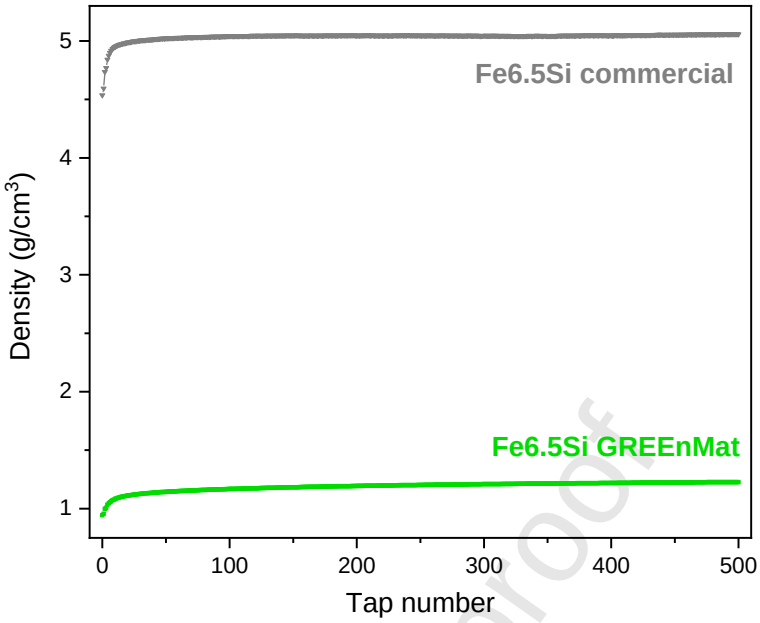


*Figure 14 : Compaction curves (density as a function of tap number) obtained with GranuPack for GREEnMat and commercial FeSi powders.*

Table 9 provides the critical coefficients for assessing flowability via compaction. The commercial powder has an Hausner ratio of 1.11, which is classified as "Excellent" flowability. In contrast, the GREEnMat powder has an Hausner ratio of 1.31, falling into the "Passable" flowability category [13]. This trend is confirmed by Carr's Index, where the commercial powder shows low compressibility (10.30%), while GREEnMat shows high compressibility (23.10%).

*Table 9 : Sample coefficients obtained with GranuPack for GREEnMat and commercial FeSi powders.*

| Coefficients | FeSi GREEnMat | FeSi commercial |
|---|---|---|
| Hausner ratio (Hr) | 1.31 | 1.11 |
| ρ[0] | 0.94 | 4.53 |
| ρ[500] | 1.23 | 5.06 |
| Carr's index (Compressibility, C) | 23.10 | 10.30 |

The high Hausner Ratio for GREEnMat likely stems from its extremely low initial bulk density. Low-density powders are often highly sensitive to air entrapment; during the GranuPack initialization, the

GREEnMat particles likely form a very loose, aerated structure. The subsequent tapping is highly effective at removing this air, leading to a large relative increase in density (high Hr).

However, the GranuDrum results prove that once the material is in a free-flowing regime, the inter-particle friction in GREEnMat is actually lower than in the commercial powder. This suggests that while GREEnMat is more "compressible," it is less "cohesive" during active handling [12,13].

The commercial powder is more stable under vibration and pressure (lower Carr's Index), making it less prone to settlement during transport. However, the GREEnMat powder displays superior dynamic characteristics (lower cohesive index in the GranuDrum), which is often the more critical factor for applications like laser powder bed fusion (LPBF), where the ability of the powder to spread into thin, uniform layers is paramount [13].

**4. Conclusions**

This study demonstrates a novel, sustainable, and scalable synthesis route for high-silicon steel (FeSi) powders by combining ATEX-compliant spray drying with reductive calcination. By utilizing recycled silicon from end-of-life photovoltaic cells, this method offers a more environmentally conscious alternative to conventional gas atomization.

The comparative analysis of three iron precursors reveals that the choice of starting material significantly dictates the final powder characteristics:

- $Fe(OH)_3$-derived powders exhibited the most robust and spherical morphology after calcination, achieving the highest calcination yield (81%) and maintaining stable secondary structures.
- $Fe_2O_3$-derived powders also maintained spherical integrity but developed high internal porosity due to the topochemical reduction process.
- $Fe(NO_3)_3 \cdot 9H_2O$-derived powders suffered from significant stickiness during spray drying and complete structural collapse during calcination, resulting in irregular, fine aggregates unsuitable for many downstream applications.

Optimized reductive calcination at 700°C for 6 hours under an atmosphere proved effective in producing phase-pure while successfully avoiding the formation of secondary phases. EDX mapping confirmed a highly uniform distribution of silicon within the iron matrix across all samples, though silicon content was slightly higher than the target at 8.2–9.4 wt%. Furthermore, Mössbauer spectroscopy confirmed that the powders are magnetically ordered and comparable to commercial standards.

The flowability and packing dynamics of a $Fe(OH)_3$-derived powder and a **commercial** powder were comprehensively characterized using GranuDrum and GranuPack instruments. The investigation

revealed a distinct difference between the static and dynamic behaviors of the two materials. While both powders showed similar flow angles, the $Fe(OH)_3$-derived powder interface remained significantly more stable and continuous, indicating lower inter-particle friction during active flow. The commercial powder possesses better static flowability indices and the higher compressibility of GREEnMat is attributed to its exceptionally low initial bulk density.

The resulting powders possess a particle size (Dv(50)) of 23.9–31.4 µm and spherical morphology required for advanced manufacturing processes such as Laser Powder Bed Fusion and Powder Injection Molding (PIM). This research establishes a versatile framework for the low-temperature synthesis of high-performance soft magnetic alloys from recycled sources.

**Author contributions**

Conceptualization, N.S., E.E. and F.C.; Methodology, N.S.; Writing – Original Draft, N.S. and A.M; Writing – Review & Editing, A.M, F.B. and R.C.

**Funding**

This research is funded by the European Regional Development Fund (ERDF) and Wallonia under the "ERDF/JTF Programme Wallonia 2021-2027".

**Conflicts of interest or competing interests**

The authors declare that they have no known competing financial interests or personal relationships that could have appeared to influence the work reported in this paper. The authors declare the following financial interests/personal relationships which may be considered as potential competing interests.

**Declaration of AI-assisted technology in the manuscript preparation process**

During the preparation of this work the author(s) used GEMINI in order to improve the language of some results descriptions. After using this tool/service, the author(s) reviewed and edited the content as needed and take(s) full responsibility for the content of the published article.

**References**

[1] V.E. Pinotti, A.F. Andreoli, M.A. Nakahashi, M. Boccalini, F.J.G. Landgraf, P. Gargarella, High-silicon electrical steel powders aimed for additive manufacturing, Powder Technol. 444 (2024). https://doi.org/10.1016/j.powtec.2024.119986.

[2] G. Ouyang, X. Chen, Y. Liang, C. Macziewski, J. Cui, Review of Fe-6.5 wt%Si high silicon steel—A promising soft magnetic material for sub-kHz application, J. Magn. Magn. Mater. 481 (2019) 234–250. https://doi.org/10.1016/j.jmmm.2019.02.089.

[3] Q. Qin, G. Li, F. Yang, P. Li, C. Chen, J. Hao, Z. Guo, Magnetic performance and microstructure characterisation of powder metallurgy Fe–6.5 wt-% Si high-silicon steel, Powder Metallurgy 65 (2022) 296–307. https://doi.org/10.1080/00325899.2021.2014650.

[4] M. Garibaldi, I. Ashcroft, N. Hillier, S.A.C. Harmon, R. Hague, Relationship between laser energy input, microstructures and magnetic properties of selective laser melted Fe-6.9%wt Si soft magnets, Mater. Charact. 143 (2018) 144–151. https://doi.org/10.1016/j.matchar.2018.01.016.

[5] O.D. Neikov, Atomization and Granulation, in: Handbook of Non-Ferrous Metal Powders: Technologies and Applications, Second Edition, Elsevier, 2018: pp. 125–185. https://doi.org/10.1016/B978-0-08-100543-9.00004-X.

[6] G. Matsagopane, E.O. Olakanmi, A. Botes, S. Kutua, Conceptual Design Framework for Setting Up Aluminum Alloy Powder Production System for Selective Laser Melting (SLM) Process, JOM 71 (2019) 1840–1857. https://doi.org/10.1007/s11837-019-03431-w.

[7] C. Jo, A.S. Groombridge, J. De La Verpilliere, J.T. Lee, Y. Son, H.L. Liang, A.M. Boies, M. De Volder, Continuous-Flow Synthesis of Carbon-Coated Silicon/Iron Silicide Secondary Particles for Li-Ion Batteries, ACS Nano 14 (2020) 698–707. https://doi.org/10.1021/acsnano.9b07473.

[8] N. Eshraghi, L. Berardo, A. Schrijnemakers, V. Delaval, M. Shaibani, M. Majumder, R. Cloots, B. Vertruyen, F. Boschini, A. Mahmoud, Recovery of Nano-Structured Silicon from End-of-Life Photovoltaic Wafers with Value-Added Applications in Lithium-Ion Battery, ACS Sustain. Chem. Eng. 8 (2020) 5868–5879. https://doi.org/10.1021/acssuschemeng.9b07434.

[9] N. Doebelin, R. Kleeberg, Profex: A graphical user interface for the Rietveld refinement program BGMN, J. Appl. Crystallogr. 48 (2015) 1573–1580. https://doi.org/10.1107/S1600576715014685.

[10] R.W. Cheary, A. Coelho, A Fundamental Parameters Approach to X-ray Line-Profile Fitting, 1992.

[11] S. Enferad, S. Pillitteri, G. Lumay, C. Gaiani, S.K. De Richter, M. Marck, S. Umbetov, N. Vandewalle, M. Jenny, Powder flow behavior governed by the surface properties of glass beads, Powder Technol. 388 (2021) 425–433. https://doi.org/10.1016/j.powtec.2021.04.101.

[12] A. Neveu, F. Francqui, G. Lumay, Measuring powder flow properties in a rotating drum, Measurement (Lond). 200 (2022). https://doi.org/10.1016/j.measurement.2022.111548.

[13] I. Baesso, D. Karl, A. Spitzer, A. Gurlo, J. Günster, A. Zocca, Characterization of powder flow behavior for additive manufacturing, Addit. Manuf. 47 (2021). https://doi.org/10.1016/j.addma.2021.102250.

[14] B. Vertruyen, N. Eshraghi, C. Piffet, J. Bodart, A. Mahmoud, F. Boschini, Spray-drying of electrode materials for lithium- and sodium-ion batteries, Materials 11 (2018). https://doi.org/10.3390/ma11071076.

[15] P. Sundararajan, J. Moser, L. Williams, T. Chiang, C. Riordan, M. Metzger, F. Zhang-Plasket, F. Wang, J. Collins, J. Williams, Driving Spray Drying towards Better Yield: Tackling a Problem That Sticks Around, Pharmaceutics 15 (2023). https://doi.org/10.3390/pharmaceutics15082137.

[16] Q. Tang, K. Huang, Determining the Kinetic Rate Constants of Fe3O4-to-Fe and FeO-to-Fe Reduction by H2, 2022.

[17] J. Vicente, J. Pinto, J. Menezes, F. Gaspar, Fundamental analysis of particle formation in spray drying, Powder Technol. 247 (2013) 1–7. https://doi.org/10.1016/j.powtec.2013.06.038.

[18] M. Takeda, T. Onishi, S. Nakakubo, S. Fujimoto, Physical properties of iron-oxide scales on Si-containing steels at high temperature, Mater. Trans. 50 (2009) 2242–2246. https://doi.org/10.2320/matertrans.M2009097.

[19] Z. Wang, B. Peng, L. Zhang, Z. Zhao, D. Liu, N. Peng, D. Wang, Y. He, Y. Liang, H. Liu, Study on Formation Mechanism of Fayalite (Fe2SiO4) by Solid State Reaction in Sintering Process, JOM 70 (2018) 539–546. https://doi.org/10.1007/s11837-017-2699-6.

[20] R.G. Pinto, A.A. Yaremchenko, M.F. Baptista, L.A.C. Tarelho, J.R. Frade, Synthetic fayalite Fe2SiO4 by kinetically controlled reaction between hematite and silicon carbide, Journal of the American Ceramic Society 102 (2019) 5090–5102. https://doi.org/10.1111/jace.16412.

[21] Z. Luo, X. Fan, W. Hu, F. Luo, J. Wang, Z. Wu, X. Liu, G. Li, Y. Li, High performance Fe-Si soft magnetic composites coated with novel insulating-magnetic-insulating (IMI) layer, J. Magn. Magn. Mater. 496 (2020). https://doi.org/10.1016/j.jmmm.2019.165937.

[22] A.D. Ritchie, M.B. Johnson, J.F. Niven, L. Haggstrom, L. Grinasl, R. Wappling, S. Devanarayanan2, Mössbauer Study of Ordering in FeSi Alloys Mossbauer Study of Ordering in FeSi Alloys, 1973.

[23] H. Danninger, C. Gierl-Mayer Dr, Advanced powder metallurgy steel alloys, in: Advances in Powder Metallurgy: Properties, Processing and Applications, Elsevier Inc., 2013: pp. 149–201. https://doi.org/10.1533/9780857098900.2.149.

[24] A.B. Spierings, M. Voegtlin, T. Bauer, K. Wegener, Powder flowability characterisation methodology for powder-bed-based metal additive manufacturing, Progress in Additive Manufacturing 1 (2016) 9–20. https://doi.org/10.1007/s40964-015-0001-4.

## Graphical abstract

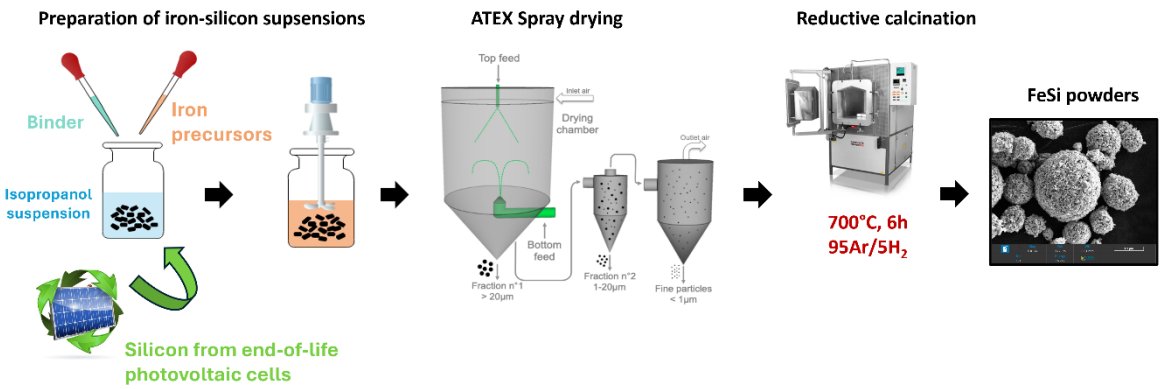

**Declaration of Interest**

The authors declare that they have no known competing financial interests or personal relationships that could have appeared to influence the work reported in this paper.

**Highlights :**

- **Methodology:** First use of ATEX-compliant spray drying for this specific alloy.
- **Sustainability:** Incorporation of recycled silicon from end-of-life PV cells.
- **Discovery:** Identification of $Fe(OH)_3$ as the optimal precursor for yield and morphology.
- **Optimization:** Achieving phase purity at the relatively low temperature of 700°C while avoiding deleterious phases like fayalite ($Fe_2SiO_4$).